

A Practical, Comprehensive Light Reflection Model

Hongsong Li and Kenneth E. Torrance

Abstract

A new comprehensive reflectance model is presented. The model accounts for both surface and subsurface local light scattering. The model combines, for the first time, highly-efficient wave optics components and rigorous empirical components. The model displays a wide range of directional and non-directional light scattering phenomena and compares favorably against extensive, detailed reflectance measurements. The model is analytic and suitable for Computer Graphics applications. Benchmark timings are comparable with that of current less comprehensive models (Lafortune, Ward, and Cook-Torrance models).

CR Categories: I.3.7 [Computer Graphics]: Three-Dimensional Graphics and Realism; I.3.3 [Computer Graphics]: Picture/Image Generation; I.6.4 [Model validation and analysis]

Keywords: reflection model, BRDF, physical measurements

1 Introduction

A major goal of computer graphics is to simulate the appearance of three-dimensional real-world scenes [GREENBERG et al. 1997]. To do this, we need to model and represent light scattering for a wide range of material surfaces, with good accuracy and reasonable computational cost. Many reflection models have been proposed to achieve this goal. However, two important problems still exist. First, the visual appearance of a surface is typically a consequence of multiple light scattering mechanisms at the surface; current models account for only part of the mechanisms. A model may work for certain materials but fail for others. Second, a good balance of accuracy and cost has not yet been reached. The most accurate models are too expensive for practical use, and the less expensive ones may fail to produce faithful renderings.

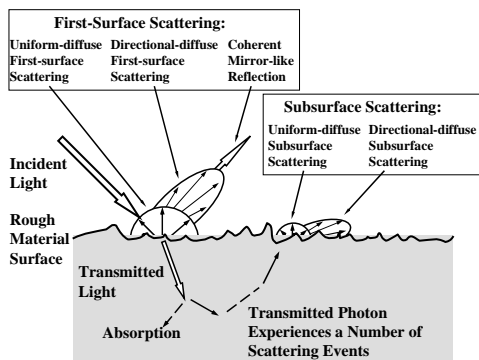


Figure 1 Light scattering processes at a surface

To address the two problems, we propose a comprehensive reflection model that includes five carefully-streamlined, analytic components, as shown in Figure 1. The components account for a wide range of light phenomena, including surface and subsurface local scattering. We do not aim to incorporate every possible optical scattering process, only a select set that has a strong influence on the quality of a rendered image. Such influences are evaluated with rendered images and physical measurements. The selected phenomena are explained physically and are individually modeled in the five components of the complete model. The components are based on wave optics, ray optics, or merely pure mathematical construction, depending on the phenomena. We also study the computational cost of each component and carefully adopt some efficient approximations. The comprehensive model compares favorably against extensive, detailed reflectance measurements. For a specific material, the components are selected and combined to build an efficient reflectance model that will yield a correct visual appearance for the material.

Before presenting our approach, we wish to state some assumptions. First, light scattering is assumed to be local so that any large volume effects of subsurface scattering are negligible. Second, the surfaces are assumed to be uniform and, if rough, rough in a random way and described well by a height field. Last, fluorescence, self-emission, and quantum effects are neglected.

Next, we present the definitions and nomenclature needed for this work.

1.1 Definitions and nomenclature

The angular and spectral dependence of local light scattering is often characterized with the Bi-directional Reflectance Distribution Function (BRDF) [NICODEMUS et al. 1977]. Bi-directional refers to the directional nature of illumination and the directional nature of reflection above a surface. Assuming that a light ray of wavelength λ arrives at and leaves a surface at the same point, the BRDF is the ratio of the radiance dL_r , reflected from a surface in the direction (θ_r, ϕ_r) to the irradiance dE_i onto the surface from the direction (θ_i, ϕ_i) , given as:

$$f_r(\lambda, \theta_i, \phi_i, \theta_r, \phi_r) = \frac{dL_r(\lambda, \theta_i, \phi_i, \theta_r, \phi_r)}{dE_i(\lambda, \theta_i, \phi_i)} \quad (1)$$

The geometry is shown in Figure 2. The incident irradiance dE_i and the reflected radiance dL_r have units of W/m^2 and W/m^2sr ; f_r has units of sr^{-1} . The BRDF is invariant to a reversal of beam directions.

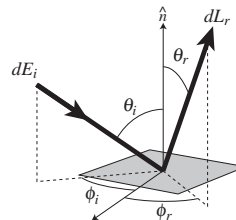


Figure 2 Coordinate system of BRDF

1.2 Previous work

There are two general approaches to simulate local light scattering on material surfaces: analytical BRDF models and BRDF representation techniques.

Analytical BRDF models can be roughly categorized into three classes: empirical models, micro-facet models, and wave optics models.

Empirical models are pure mathematic constructions without a theoretical basis. In 1975, Phong introduced an empirical model that dramatically improved the richness and realism of rendered images [PHONG 1975]. The model was designed to reproduce a glossy effect with minimal computation. Until today, this model and its variations are still the most important and widely used BRDF models in the CG community. Subsequently, this model has been extended to incorporate more features such as reciprocity [BLINN 1977], energy conservation [NEUMANN et al. 1999], and anisotropy [ASHIKHMIN and SHIRLEY 2000]. The empirical models are compact and computationally efficient. But they may fall short in reproducing the exact reflectance of a surface.

Micro-facet models are based on ray optics. The surfaces are modeled as a collection of micro-facets. The statistical properties of the micro-facets were exploited to give analytical solutions for the angular distribution of scattered light. One of the first models of this class was developed by Torrance and Sparrow, aiming to describe the off-specular peak of the BRDF on a rough surface [TORRANCE and SPARROW 1967]. Later, Cook and Torrance [COOK and TORRANCE 1981] proposed a similar model with better accuracy, based on Beckmann's work [BECKMANN 1963]. Ward simplified the Cook-Torrance model for better efficiency and importance sampling, and extended the model for anisotropic surfaces [WARD 1992]. Oren and Nayar [OREN and NAYAR 1994] presented a micro-facet model for extremely rough surfaces which have steep RMS slopes and show strong backscattering. These models have better accuracy and incorporate more phenomena than the empirical BRDF models.

The wave optics models are the most complete and accurate BRDF models, applicable to a wide range of materials and roughness conditions. Beckmann [BECKMANN 1963] proposed one of the first wave optics models based on the scalar form of the Kirchhoff theory. Stogryn [STOGRYN 1967] extended the model with the vector form of the Kirchhoff theory. He et al [HE et al. 1991] proposed the first wave optics BRDF model in the CG community. The model was developed based on the works of Stogryn and Smith [SMITH 1967]. Later, Stam [STAM 1999] developed another wave optics BRDF model based on the scalar form of the Kirchhoff theory and extended the model for anisotropic surfaces. Although the accuracy of these models is superior to any other models based on comparisons with physically-measured BRDF data, they are rarely used in practice due to their complexity and high computational cost.

BRDF representation techniques are usually mathematical constructions for data fitting. The most popular representation techniques are spherical harmonics [SILLION et al. 1991; WESTIN et al. 1992], Zernike polynomials [KOENDERINK and DOORN, 1998], and spherical wavelets [SCHRÖDER and SWELDENS 1995]. Kautz and McCool [KAUTZ and MCCOOL 1999] have represented the BRDF as a sum of separable functions. Although these techniques are theoretically capable of representing any BRDF exactly, they require many coefficients to

achieve a good approximation of a typical BRDF, as compared to several coefficients for the analytical parameterized models. Lafortune et al. [LAFORTUNE et al. 1997] generalized the Phong model with multiple cosine lobes. This model sacrifices the complete generality of other models in this category, but is much simpler and more compact. Matusik et al. [MATUSIK 2003] enumerated the entire space of BRDFs occurring in the real world and extracted a relatively small number (15-30) of basis functions to span the space. In practice, these general representations must be fitted to data from another source: either a physical model or measured data.

2 From optics to appearance

In this section, we summarize the physics of local light scattering as it impacts the appearance of material surfaces. The local light scattering comes from first-surface and subsurface scattering, as shown in Figure 1. "First-surface scattering" refers to scattering that occurs at a material surface. The light scattering on metal surfaces is completely first-surface scattering, since essentially no electromagnetic waves penetrate the surface. For dielectric materials, part of the incident energy crosses the surface. A portion of the transmitted light energy can be scattered within the material and again be transmitted across the surface. We refer to this as "subsurface scattering." We next discuss these processes and how they can be modeled.

2.1 First-surface scattering

2.1.1 Smooth surfaces and Fresnel reflection coefficients

The simplest case of first-surface scattering is a perfectly smooth surface that exhibits ideal mirror reflection. This is also called coherent reflection, because there is a phase coherence between the incident and reflected beams. A surface is considered to be smooth when its roughness features are significantly smaller than the incident wavelength. The reflection from such smooth surfaces is given by the Fresnel formulae, which predict that the reflectance of a smooth surface depends only on the incidence angle and the optical properties of the material (the refractive index n).

The Fresnel reflection coefficients of metals and dielectrics are quite different in terms of their angular dependence and magnitude, giving metals and dielectrics very different visual appearances. Reflection from a smooth metal surface is relatively independent of angle, while a dielectric has a low reflectance over most of the angular range with a steep increase near grazing incidence. Polished metals show a reflectance of over 50% for all angles, while most smooth dielectrics fall well below 20% for the majority of the range. A BRDF model should incorporate the Fresnel reflection coefficient to correctly describe the angular dependence. Many researchers, including Shirley [SHIRLEY et al. 1997] and Neumann [NEUMANN et al. 1999], have discussed the importance of the Fresnel reflection coefficient.

2.1.2 Rough surfaces

Rough surfaces can scatter incident light into the entire reflection hemisphere above the surface, instead of just into the mirror direction. The angular distribution of the scattered light depends strongly on the surface roughness. Usually, the surface roughness

is described statistically by the RMS roughness height σ and the horizontal autocorrelation length τ . The light scattering behavior can be categorized by the ratio of the roughness height σ to either the horizontal length τ or the incident light wavelength λ .

Mirror-like rough surfaces ($\sigma < \lambda$)

Surfaces with roughness smaller than the incident wavelength ($\sigma < \lambda$) have similar behavior to perfectly smooth surfaces, but their specular reflectance is attenuated by a well-known relationship [DAVIES 1954]:

$$\rho_{sp} = F \exp\left[-(4\pi \frac{\sigma}{\lambda} \cos \theta_i)^2\right] \quad (2)$$

where ρ_{sp} is the resulting specular reflectance, F is the Fresnel reflection coefficient, and σ is the RMS roughness. The rest of the reflected light energy is generally scattered to the hemisphere above the surface. The specular, mirror-like reflection in (2) cannot be neglected or treated as smooth mirror reflection, because the mirror-like reflection on such a surface appears gradually at grazing angles of view, as shown in Figure 3.

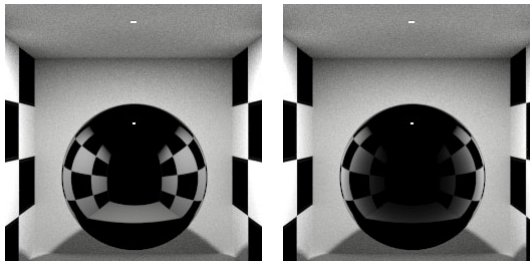


Figure 3 The left sphere was rendered as a smooth mirror. The right sphere was rendered as specular, mirror-like reflection from a rough surface ($\sigma/\lambda=0.2$).

Slightly rough surfaces ($\sigma \approx \lambda$)

For a slightly rough surface with roughness close to the incident wavelength, the reflection behavior is a smooth transition from specular to directional-diffuse. Varying the angle of incidence, the magnitude and the angular distribution (i.e., the shape of the lobe) of the BRDF varies dramatically. Physically, such surfaces can only be handled by a wave optics model. However, the empirical models and the micro-facet models can, under certain conditions, produce rendered images with decent quality for such surfaces, because most reflected light is near the specular direction and is well described by a symmetric lobe. Subtle differences might be observed at high grazing angles of view. However, human vision may be saturated by the high dynamic range of the reflection and miss the difference. Thus, most available BRDF models have good performance in rendering such glossy, slightly rough surfaces.

Moderately rough surfaces ($\sigma \gg \lambda$)

Moderately rough surfaces have a roughness size much greater than the incident light wavelength. The wave nature of light is negligible. The micro-facet models have similar performance here to the wave optics models but are more efficient. For such surfaces, the first-surface scattering often takes the form of a smooth lobe at, near, or slightly beyond the specular direction. With increasing roughness, the angular variations of the BRDF can be milder and for moderate angles of incidence the lobes can approach Lambertian.

Empirical models based on one or more cosine lobes fall short in predicting the angular distribution of the BRDF for such surfaces. In Figure 4, we compare the BRDFs predicted by several cosine-

lobe based BRDF models and by the He-Torrance model, for incident directions of 10° , 40° , and 70° and a wavelength of 550nm. The predicted hemispherical BRDFs were mapped onto a square [SHIRLEY and CHIU, 1994]. The mapping guarantees that each grid element in the plot represents a region of the hemisphere with the same solid angle. The vertical axis is the BRDF; the left and right orthogonal axes map the spherical coordinates above a surface. The plane of incidence goes through the peaks. The sampling positions were uniformly distributed to capture the basically diffuse character of this surface. The mapping is responsible for the sharp-edged artifacts along the diagonals; they do not exist in the data. The wave-optics model generates correct angular distributions. The cosine lobes generate incorrect off-plane distributions (wider lobes) and incorrect BRDF maxima at large angles of incidence, resulting in an incorrect shape and position of the reflection pattern on rendered surfaces. With a relatively low magnitude of reflection, the errors in the predicted angular distribution are visible in an image. In Section 5, we illustrate the errors with rendered images of such a rough surface.

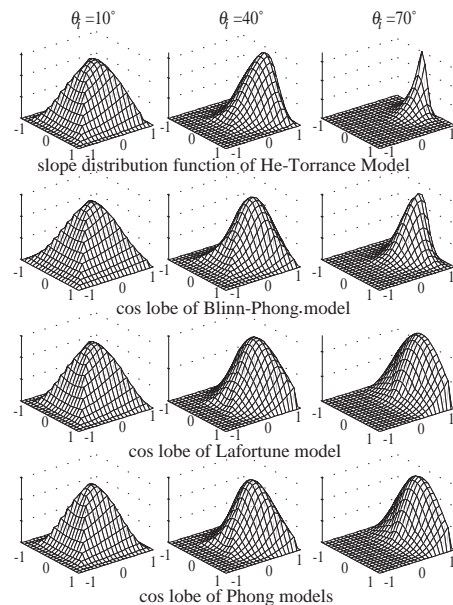


Figure 4 Comparing the angular distributions of BRDFs predicted by the cosine-lobe based empirical models and by the He-Torrance model.

Extremely rough surfaces ($\sigma/\tau > 0.2$)

Extremely rough surfaces such as sandpaper are not well matched by Lambertian or micro-facet models. The surfaces have a large mean surface slope, violating the assumptions of these models. The large slope produces strong backscattering at grazing angles of illumination. Oren and Nayar have developed a model for this case [OREN and NAYAR 1994]. Our reflection model does not cover this case, but the model can be easily incorporated into our framework as a BRDF component.

2.1.3 Geometrical factors

Some geometrical factors, such as the shadowing/masking effect and the effective roughness, also have significant impact on the visual appearance, especially for rough materials. They are macroscopic effects that are best modeled with ray optics.

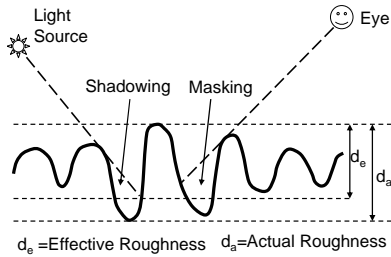


Figure 5 Shadowing/masking and effective roughness

When the surface is rough, part of the roughness valleys can be occluded for both illumination and viewing, reducing the amount of light reflection. This is the shadowing/masking effect, which is especially obvious at large angles of incidence and reflection. A general solution is to correct the predicted BRDF with a multiplicative shadowing/masking function, which describes the angular dependence of the portion of the surface area that is both illuminated and viewed. While the shadowing/masking effect reduces the illuminated/viewed area, it also reduces the surface roughness that effectively participates in the scattering process. As a result, at large angles of incidence and reflection, rough surfaces behave as though their roughness is smaller than the actual roughness of the surface. To account for the effect, the RMS roughness needs to be replaced by an effective roughness, which depends on the angles of incidence and reflection. At large angles, the effective roughness can be significantly smaller than the RMS roughness. The overall effect of these two geometrical factors is that at large angles of incidence and reflection, the light scattering is weaker but glossier.

2.1.4 Composition of roughness scales

Real-world surfaces are rough at all length scales. Therefore, for a rough surface, all the cases mentioned above could co-exist at the same time. From BRDF measurements of a rough surface, we often observe the light scattering behavior of more than one roughness scale. Many graphics practitioners have realized this problem, including Kajiyama [KAJIYAMA 1985] and Cook [COOK and TORRANCE 1981]. In general, the roughness scales comparable to the incident wavelength dominate the directional-diffuse scattering. The larger roughness scales make their contributions to the total scattering behavior by varying the surface normal, shadowing, and masking.

2.2 Subsurface scattering

Subsurface scattering is complex, given that the incident light experiences more than one scattering event, at the interface and inside the volume. Local subsurface scattering (with a negligible volume size effect) is often modeled as a Lambertian BRDF. The angular dependence of the volumetric subsurface scattering is then assumed to be negligible, since the directionality of the incident light disappears after many scattering events. However, as pointed out by Wolff [WOLFF et al. 1998], the angular dependence of the outgoing transmission should be accounted for. Assuming a smooth interface, the transmissions can be predicted with the Fresnel transmission coefficients. The Fresnel formula predicts that the transmittance from air into a smooth dielectric drops dramatically beyond 60° incidence. Meanwhile, the Fresnel reflection coefficient for reflection from the surface of increases, enabling first-surface scattering to dominate subsurface reflection at large angles of incidence.

On the other hand, the volumetric subsurface scattering can be directional. Granberg [GRANBERG 2003] observed a distinct forward scattering from paper sheets at angles much larger than the specular direction, mainly due to the structural shape and distribution of the paper fibers. In reality, a portion of the volumetric subsurface scattering is always directional. However, at the first surface (see Figure 1), there is also a forward scattering due to first-surface reflection, which has been reported by Torrance and Sparrow [TORRANCE and SPARROW 1967]. To separate the directional surface and subsurface scattering, we measured the polarized BRDF of a sheet of laser paper. The incidence-plane BRDFs arising from subsurface scattering are shown in Figure 6 for various angles of incidence. The subsurface scattering cannot be considered Lambertian.

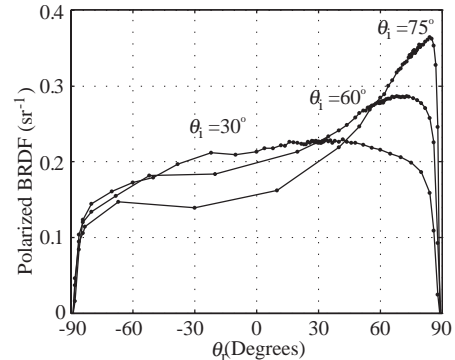


Figure 6 Measured polarized BRDF of Laser Paper Sample #73 at 550nm wavelength.

Directional subsurface scattering has several unique features: off-specular peaks always emerge at grazing angles of reflection for large angles of incidence; the magnitude increases dramatically; the scattered light is more de-polarized and spectrally selective.

From the foregoing review of light scattering phenomena on a material surface, due to surface and local subsurface processes, we conclude that no general mathematical construction can, at present, describe all of the phenomena. We therefore propose a framework consisting of several separate components (in total, five) that model the different phenomena. To simulate the appearance of a specific material surface, a BRDF model can then be assembled with relevant selected components.

3 BRDF model for local light scattering

We now propose a comprehensive reflection model for simulating local light scattering. We include five BRDF reflection components. They are a specular mirror-like component, a first surface directional-diffuse component, a first surface uniform-diffuse component, a subsurface uniform-diffuse component, and a subsurface forward-scattering component. The components are described in the following subsections. Isotropic surfaces are assumed; the extension to anisotropic surfaces appears in the Appendix. Further details on the model and the associated BRDF measurements are available in a forthcoming dissertation [Li 2005]. In the following, the key equations of the reflectance model are (3), (9) and (11)-(13). Those wishing to proceed directly to renderings may skip to Section 4.

The coordinate system is shown in Figure 7. N is the unit vector of the surface normal; L is the unit vector of the illumination

direction; V is the unit vector in the viewing direction; H is the unit vector of the bisector direction of L and V ; θ_b is the zenith angle between the surface normal and the bisector direction; θ_h is the zenith angle between the bisector direction and the viewing direction; and ϕ_b is the azimuthal angle between the surface normal and the bisector direction.

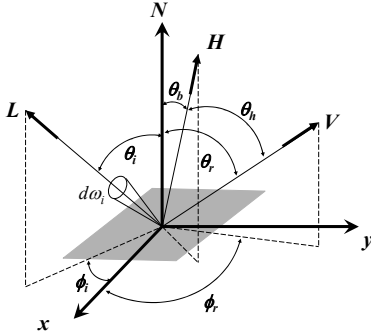


Figure 7 Coordinate configuration of the reflection model

3.1 Specular reflection component

The coherent, specular component models the light scattering behavior of a mirror-like rough surface. We use the specular component of the He-Torrance model with a scale factor, given as

$$f_{r,coh} = k_{dd}(\lambda) \frac{F \cdot S \cdot \exp(-g)}{\cos \theta_i \cos \theta_r} \cdot \Delta \quad (3)$$

where $k_{dd}(\lambda)$ is the user-specified scale factor, which equals the directional-hemispherical reflectance of both the directional-diffuse scattering and the specular scattering; F is the Fresnel reflectance; S is the shadowing/masking function; g is the apparent roughness given as

$$g = \left[\frac{2\pi\sigma_e}{\lambda} (\cos \theta_i + \cos \theta_r) \right]^2 \quad (4)$$

where $d\omega_i$ is the solid angle of the incident light; Δ is the delta function in the specular direction; and σ_e is the effective roughness. To reduce the computational cost, approximation functions are used to calculate F , S , and σ_e (equations (5), (6) and (8) below).

The Fresnel reflection coefficient F is evaluated with Schlick's approximation [SCHLICK 1994]:

$$F(\lambda, \theta_h) = f_\lambda + (1 - f_\lambda)(1 - \cos \theta_h)^5 \quad (5)$$

where f_λ is the spectral Fresnel reflectance at normal incidence. The approximation has low relative error (less than 2%). Note that the Fresnel reflectance is evaluated at θ_h (or the half angle).

Smith's [SMITH 1967] shadowing/masking function was adopted by He et. al. and was proved to be sufficiently accurate. We propose a numerical approximation for the function, given as:

$$S(\sigma, \tau, \theta_i, \theta_r) = [1 - (1 - \cos \theta_i)^{\tau/\sigma}] \cdot [1 - (1 - \cos \theta_r)^{\tau/\sigma}] \quad (6)$$

The equation approximates the dependence of the shadowing/masking function on angle and roughness features. At large angles ($\cos \theta \approx 0$), S approaches 0; while at normal incidence ($\cos \theta = 1$), $S = 1$. The RMS slope σ/τ controls the rate at which S drops. A large slope makes S drop more quickly. Smith's function and our approximation are compared in Figure 8 at

various angles of incidence. Schlick [SCHLICK 1994] also proposed an approximation for the shadowing/masking function, S_s and that is included in the figure. Our simple approximation agrees well with the exact results of Smith's shadowing/masking function. A second advantage is that it allows a prediction of the angles (of incidence or reflection) where the shadowing/masking effect becomes apparent. With a simple derivation, we have:

$$\text{If } \cos \theta_i > (1 - 0.005^{\tau/\sigma}) \text{ and } \cos \theta_r > (1 - 0.005^{\tau/\sigma}), S > 0.99. \quad (7)$$

When satisfied, we set $S = 1$, thus accelerating a computation.

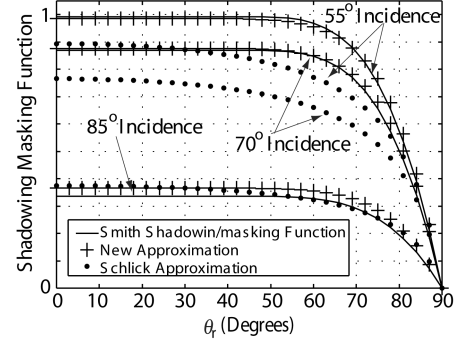


Figure 8 Shadowing/masking functions vs. angle of reflection; $\sigma = 0.5 \mu\text{m}$, $\tau = 2.5 \mu\text{m}$

An effective roughness appears in the He-Torrance model; we propose a simpler numerical approximation:

$$\sigma_e = \sigma \left\{ [1 - (1 - \cos \theta_i)^{1.6\tau/\sigma}] \cdot [1 - (1 - \cos \theta_r)^{1.6\tau/\sigma}] \right\}^{0.1\tau/\sigma} \quad (8)$$

The exact and approximate forms are shown in Figure 9 for three angles of incidence. The two sets of curves are very similar, except when the incidence and reflection angles are greater than about 85°.

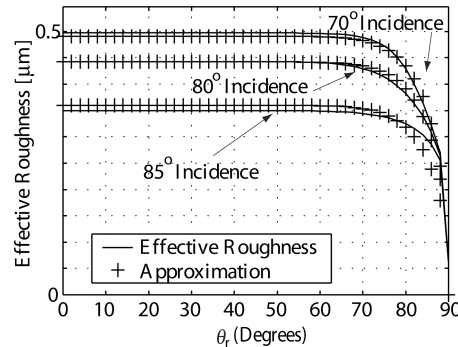


Figure 9 Effective roughness functions vs. angle of reflection; $\sigma = 0.5 \mu\text{m}$, $\tau = 3 \mu\text{m}$.

3.2 First surface directional-diffuse component

We use the directional-diffuse term of the He-Torrance model with a scale factor as our first surface directional-diffuse component:

$$f_{r,dd} = k_{dd}(\lambda) \frac{F \cdot S \cdot D}{\pi \cos \theta_i \cos \theta_r} \quad (9)$$

where $k_{dd}(\lambda)$ is the same parameter appearing in (3) and D is a slope distribution function. The D term of the He-Torrance model is very complex and expensive, preventing the model's use for

realistic CG applications, but it is the D term that largely accounts for the good accuracy of the He-Torrance model when compared against measured BRDFs.

After extensive studies of the D term and comparison of predicted BRDFs with measured BRDFs, we conclude that a simpler rough surface approximation for D is often sufficiently accurate. Formally, when the apparent roughness $g \gg 1$, the He-Torrance D term becomes:

$$D = \left(\frac{\bar{\mathbf{v}} \cdot \bar{\mathbf{v}}}{\bar{\mathbf{v}} \cdot \mathbf{N}} \right)^2 \frac{1}{16m_e^2 (\cos \theta_i + \cos \theta_r)^2} \exp\left(-\frac{\tan^2 \theta_b}{4m_e^2}\right) \quad (10)$$

where $\bar{\mathbf{v}}$ is the wave vector change given as $\bar{\mathbf{v}} = 2\pi(L+V)/\lambda$; m_e is the effective slope that is the ratio of the effective roughness σ_e to the autocorrelation length τ . The D term in equation (10) is a function of the slope σ/τ , whereas the general D term in the He-Torrance model is a function of σ and τ . The visual impact of this simplification appears to be generally small. This is demonstrated by a comparison of the model with BRDF measurements on a slightly rough metal surface in Section 5.2.1. For smoother surfaces, as g approaches 1, the error due to the approximation is even smaller.

3.3 First surface uniform-diffuse component

The first surface uniform-diffuse BRDF component accounts for multiple scattering on rough surfaces. We have observed this BRDF component for many rough metal surfaces. The angular dependence of the multiple scattering often appears to be very close to Lambertian. Then the component is simply given by:

$$f_{r,udf} = \frac{k_{udf}(\lambda)}{\pi} \quad (11)$$

where $k_{udf}(\lambda)$ is the directional-hemispherical reflectance due to the multiple scattering, and which is either specified by the user or found from physical measurements.

3.4 Subsurface uniform-diffuse component

The subsurface uniform-diffuse component is given by:

$$f_{r,uds} = \frac{k_{uds}(\lambda)}{\pi} T(\theta_i, n_\lambda) T(\theta_r, n_\lambda) \quad (12)$$

where $k_{uds}(\lambda)$ is the directional-hemispherical reflectance due to the subsurface uniform-diffuse scattering and T is the Fresnel transmission coefficient. We use Schlick's approximation to calculate the Fresnel transmission coefficient T , since $T=1-F$. $k_{uds}(\lambda)$ is often specified by users as a function of the materials or extracted from physical measurements. To be able to enforce energy conservation, $k_{dd}(\lambda)$, $k_{udf}(\lambda)$, and $k_{uds}(\lambda)$ must always be smaller than 1.

3.5 Subsurface forward-scattering component

The Torrance-Sparrow, Cook-Torrance, and He-Torrance models all describe a directional-diffuse forward-scattering that results from first-surface reflections (see Section 3.2). They did not study similar directional effects produced by subsurface scattering. When attempting to fit the aforementioned models to measured BRDFs for surfaces with subsurface forward scattering, we found

that the forward-scattering was not well predicted. That is, there was an apparent difference in shape between first surface directional-diffuse and subsurface forward scattering. Since we are not aware of any model for subsurface directional forward scattering, we here propose an empirical BRDF model. The model is based on functional reasoning and our data fitting experience [Li 2005].

$$f_{r,fs} = \frac{k_{fs}(\lambda)}{\pi} T(\theta_i, n_\lambda) T(\theta_r, n_\lambda) (1 - \cos \theta_i) (1 - \cos \theta_r) \exp\left(-\frac{\tan^2 \theta_f}{16m_e^2}\right) \quad (13)$$

where $k_{fs}(\lambda)$ is a user-specified free parameter that determines the magnitude of the subsurface forward scattering and

$$\theta_f = \cos^{-1}\left(\frac{V \cdot [N(N \cdot L) - L]}{|N(N \cdot L) - L|}\right) \quad (14)$$

The component approximates quite well our observed dependences on angle, optical properties, and roughness features.

4 Guidelines to assemble a BRDF for specific surfaces and a rendering example

The new reflection model contains five terms to account for mirror-like reflection and first-surface and subsurface directional and uniform scattering (equations (3), (9), (11)-(13)). For real-world surfaces, not all the BRDF components may be needed. For example, a very rough surface has no specular reflection; smooth surfaces have no first-surface directional or uniform scattering; metallic surfaces have no subsurface scattering; but a rough dielectric may have all of the first-surface and subsurface scattering components. It may be helpful to offer a few guidelines for the construction of BRDF models for specific materials using the five terms. Visual inspection of the materials often helps.

- A. If mirror reflection eventually emerges at large angles of illumination, the specular mirror-like component should be included.
- B. For rough surfaces, the first surface directional-diffuse component is needed, except when the reflection displays no visual evidence of angular variations (i.e., perfectly diffuse).
- C. The shadowing/masking function and the effective roughness are negligible for smooth or slightly rough surfaces.
- D. The Fresnel reflectance is absolutely necessary for dielectric surfaces, but somewhat negligible for metal surfaces if computational cost is a factor.
- E. The first surface uniform-diffuse reflection component is only needed for rough metal surfaces. For rough dielectric surfaces, the subsurface uniform-diffuse component usually dominates and is used instead.
- F. For the subsurface forward-scattering component on dielectrics, in the absence of physical measurements, we cannot offer simple guidelines.

After assembling appropriate components of the reflection model for a particular material surface, five or fewer adjustable coefficients appear, including the roughness lengths σ and τ . The factor $k_{dd}(\lambda)$ scales the magnitude of the two terms that come from the wave optics model of He-Torrance; the factor appears for two possible reasons: first, the surface may contain impurities and contamination (generally true for real-world surfaces); second, with moderate to large roughness values there may be secondary reflections on the surface. We have found it convenient to use the

directional hemispherical reflectance as the scaling coefficient (measurable with a diffuse reflectometer), and to further scale down the coefficient to account for uniform diffuse reflection ($k_{udf}(\lambda)$ or $k_{uds}(\lambda)$) if it should exist. In the latter case, a diffuse reflectometer would provide only the sum of $k_{ad}(\lambda)$ and the uniform-diffuse coefficient ($k_{udf}(\lambda)$ or $k_{uds}(\lambda)$).

All five coefficients can also be found by fitting the model to measured BRDFs (see Section 5). However, many times simple estimates of the required coefficients may be sufficient. For example, by understanding the characteristics of the five light scattering processes included in the model, we are often able to select the right reflection components and determine the input coefficients with several test runs. Figure 11 provides a comparison of a photograph and a rendering. There are five surfaces in the image. We were able to achieve a reasonable visual match by selecting the model components for each surface and then simply adjusting the parameters.

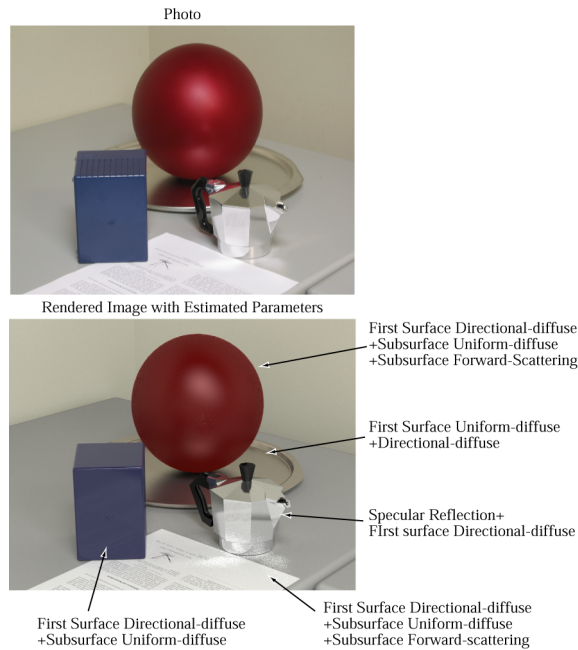


Figure 11 A rendering example

5 Evaluation of model against physical measurements

The preceding sections describe the reflection model, the physical basis of its five components, and some rendering guidelines. A significant question remains, and that involves the fidelity or accuracy of the model with respect to the five components. That question is best answered by comparisons with detailed reflectance measurements. In this section, we do such a comparison, on material surfaces that display the five reflection components, singly, in pairs, or in various combinations.

5.1 Approach

Many surfaces were studied but we present results only for four surfaces. The surfaces are aluminized non-glare glass, aluminized ground glass, garnet red paint, and laser paper. The samples are

isotropic, uniform, and at least 4 inch by 4 inch square to allow full hemispherical BRDF scans.

The BRDFs were measured with an automated three-axis gonireflectometer [FOO 1997; LI and TORRANCE 2003]. The angular range covers the entire incidence and reflection hemispheres to an angle of 85°, with the exception of a 7° cone around retro-reflection. The instrument covers the visible spectrum (400nm-700nm) with high wavelength resolution. We obtain 31 convolved wavelength samples in one snapshot. We also convert them to RGB values. Measurements take about 11 hours for full hemispherical sampling.

Two sampling methods were used: incidence-plane sampling and hemispherical sampling. The former method uses a non-uniform distribution of sampling points, with more points near the specular direction. The method was used to characterize the smoother surfaces for which the variation of the BRDF near the specular direction is strong. The angles of incidence are 15°, 30°, 45°, 60°, and 75°. The number of sampling points in a scan ranges from 40 to 70. The hemispherical sampling method uses uniformly-distributed sampling positions over the hemisphere. It is used for rough surfaces with mild angular variations of the BRDF, so that sparse sampling is able to resolve the scattering pattern. The angles of incidence vary from 10° to 80°, with a 10° interval. For each angle of incidence, we use 441 sampling positions over the reflection hemisphere.

We used the non-linear optimization tool from Matlab for fitting the parameters of a BRDF model to the measured data. Depending on the number of free parameters to be found, either Quasi-Newton or Trust-region methods were used. The tool finds the combination of free parameters that produces the minimum fitting error. The fitting error is the difference between a predicted and a measured BRDF. We use an L2 norm weighted with the cosine of the incidence angle.

$$\Delta f_r = \sum_j \sum_{k=1}^n \cos(\theta_{i,k}) \left| \sum_{m=1}^p [f_{r,mod}(\lambda_j, \theta_{i,k}, \theta_{r,m}, \phi_{r,m}) - f_{r,mea}(\lambda_j, \theta_{i,k}, \theta_{r,m}, \phi_{r,m})] \right|^2 \quad (15)$$

where n is the number of incidence angles; p is the number of sampling points for each angle of incidence, $f_{r,mod}$ is the predicted BRDF from a BRDF model, and $f_{r,mea}$ is the measured BRDF. For the incidence-plane sampling and BRDF fitting, $\phi_{r,m} = 0$. The cosine weight gives more weight to BRDF values at small angles of incidence, and thus is weighted by the incident-energy surface flux.

5.2 Case studies

5.2.1 Aluminized Non-glare Glass, Sample #45

This sample is a piece of 5 inch by 5 inch square non-glare glass. The glass was roughened by erosion to eliminate glare. We deposited pure aluminum on the glass to form an aluminum coating of at least 500nm thickness. The pure aluminum coating makes it easy to determine the index of refraction. The coating is thick enough to be opaque, consequently eliminating any subsurface scattering. The sample displays a smooth transition from directional-diffuse scattering to mirror reflection. The sample illustrates the role of specular reflection on a mirror-like rough surface.

To construct a BRDF model for this surface, we neglect all subsurface scattering and first surface uniform-diffuse scattering. Only the first two terms of the reflection model remain, those due to specular and first-surface directional-diffuse reflection. In addition, the shadowing/masking function and the effective roughness can be neglected. Thus, the resulting BRDF model is

$$f_r = f_{r,dd} + f_{r,coh} = \frac{F}{\cos \theta_i} \cdot \left[\frac{D}{\pi \cos \theta_r} + \frac{\exp(-g)}{d\omega_i} \cdot \Delta \right] \quad (16)$$

The effective roughness σ_e is replaced by the RMS roughness σ . We set the scale factor k_{dd} to unity for this pure (uncontaminated) aluminum surface with moderate roughness slopes (thus no multiple scattering). The model thus directly provides the absolute magnitude of the BRDF. $d\omega_i$ was tentatively set as 0.0005, which is the estimated solid angle of the experimental light source. The constructed model (essentially the He-Torrance model) depends on only two free parameters, the RMS roughness σ and the autocorrelation length τ . The results from the fitting algorithm yield $\sigma=0.23\mu\text{m}$, $\tau=9.9\mu\text{m}$. Fitting results for the complete He-Torrance model (i.e., no speed-up approximations) yield $\sigma=0.23\mu\text{m}$, $\tau=10.4\mu\text{m}$. The best-fit BRDF curves for the present model and for the full He-Torrance model, for three color channels, are shown in Figure 12.

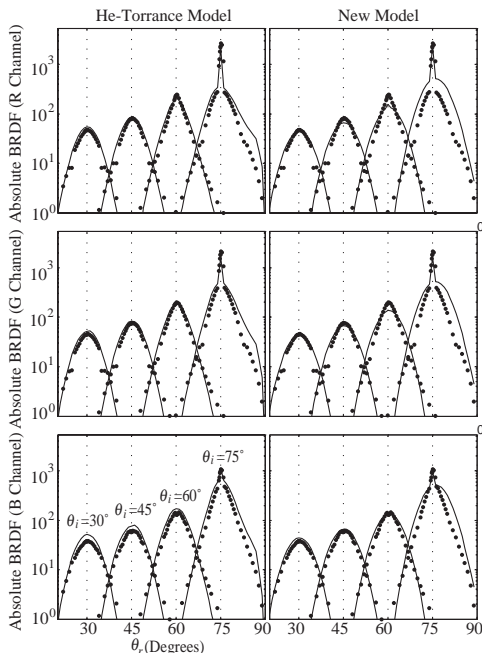


Figure 12 Comparison of best-fit curves for two BRDF models with measured BRDFs for Aluminized Non-glare Glass #45.

The black dots are the measured BRDFs. The ordinate is the absolute value of the BRDF in logarithmic scale. The abscissa is the zenith angle of reflection. All the figures use the same scales in both axes to allow inter-comparisons. Limited by space, we show measured BRDFs and fitted curves for only four angles of incidence (30°, 45°, 60°, and 75°), see curve labels at bottom left.

The measured BRDFs display a phenomenon that can only be predicted by wave optics. Namely, a specular component appears, at 75° incidence, and is larger in magnitude in the R channel than in the B channel. The wave nature of light makes the surface appears smoother at the longer wavelength. The new model and the He-Torrance model, with only two free parameters,

accurately predict the appearance of the specular, mirror-like reflection, as well as its spectral dependence.

The first surface directional-diffuse component of the new model is less accurate than that of the He-Torrance model. This is due to the rough surface approximation of the slope distribution term D that is adopted in the new model. Nevertheless, the difference in a rendered image will be negligible, due to the high dynamic range of the BRDF directional-diffuse component.

5.2.2 Aluminized Ground Glass, Sample #4

This sample is a piece of 5 inch by 5 inch window glass, ground with SiC grinding powder (120grit), and coated with a pure aluminum film. The grinding process generated a uniform, isotropic surface. The sample illustrates the importance of correctly predicting the angular distribution of the BRDF for a slightly to moderately rough surface.

For such a surface, the specular reflection is negligible. In addition, the rough surface scatters a fraction of the incident light uniformly to the reflection hemisphere. We now construct a BRDF model which includes the first-surface uniform-diffuse and directional-diffuse components, given as:

$$f_r = f_{r,udf} + f_{r,dd} = \frac{k_{ud}}{\pi} + k_{dd} \frac{F \cdot S \cdot D_r}{\pi \cos \theta_i \cos \theta_r} \quad (17)$$

The effective roughness and the shadowing/masking function are included. The scale factor k_{dd} in the directional-diffuse component accounts for energy loss on the rough metal surface. We also use the same scale factor in the He-Torrance model when doing comparisons. The constructed model and the He-Torrance model are functions of four free parameters: k_{ud} , k_{dd} , σ , and τ .

Unlike the smoother metal surface in the previous section, the angular variation of the BRDF is less concentrated and dramatic. Incidence-plane sampling is no longer sufficient to fully characterize the reflection pattern. We used the hemispherical sampling method for the measurements and fitted the selected model over the entire reflection hemisphere. The fitting results are listed in Table 1.

Table 1 Summary of best-fit results for Aluminized Ground Glass #41

Models	Param.	Fitting Results		
		R	G	B
He-Torrance	k_{ud}	0.32	0.32	0.31
	k_{dd}	0.47	0.47	0.46
	$\sigma [\mu\text{m}]$	0.90		
	$\tau [\mu\text{m}]$	5.2		
Constructed Model	k_{ud}	0.33	0.34	0.32
	k_{dd}	0.45	0.44	0.44
	$\sigma [\mu\text{m}]$	0.86		
	$\tau [\mu\text{m}]$	4.99		

The measurements show almost no spectral dependence, so we chose just one color channel, G, for analysis. Measured and best-fit BRDFs are shown in Figure 13. The rows correspond to five incidence angles, namely, 20°, 40°, 50°, 70°, and 80°. The figures in each row share the same scale on the vertical axis.

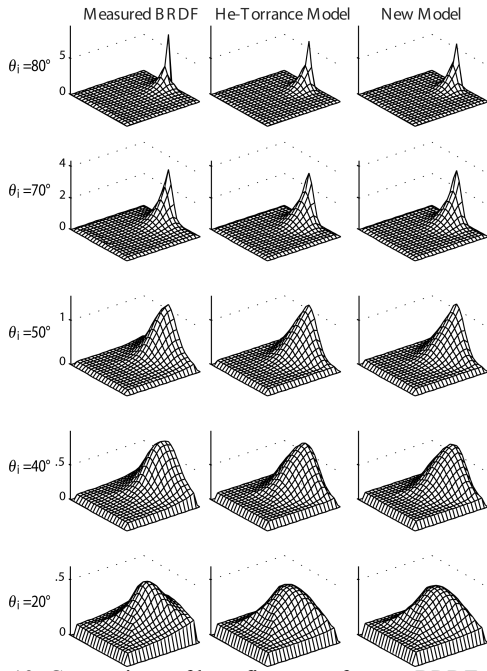


Figure 13 Comparison of best-fit curves for two BRDF models with measured BRDFs for Aluminized Ground Glass #41; G channel.

The measured BRDFs clearly show the presence of two first-surface reflection components: directional-diffuse and uniform-diffuse. The strong directional variations (shape) are due to the directional-diffuse component. The uniform-diffuse component accounts for the regions of constant vertical height. The constant vertical offset in the BRDF exists for all incidence angles; its magnitude is almost independent of the angles of incidence and reflection (except at grazing angles), a property consistent with Lambertian, diffuse behavior. The vertical offset is more apparent at larger angles of incidence due to the relative scales. The large directional variations of the directional-diffuse component provide a highly discriminating test of the physical correctness of a BRDF model.

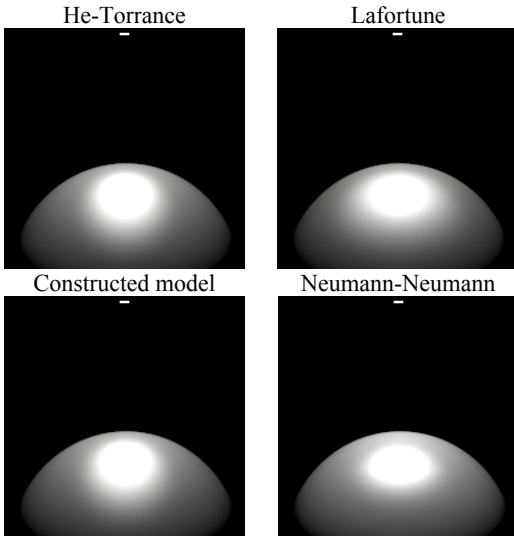


Figure 14 Comparison of rendered images for four BRDF models

Both BRDF models give good predictions. The directional distributions match the physical measurements quite well. To provide further comparisons, the Lafortune and Neumann-Neumann models were also fitted to the same measured BRDFs. The fitting results for all four models were then used for rendering a sphere illuminated by an overhead point light source. The rendered comparison images are shown in Figure 14.

This simple rendering illustrates the importance of correct predictions of the angular distribution of the BRDF, particularly for the directional-diffuse term. The bright spots predicted with cosine lobe models have incorrect positions and shapes.

5.2.3 Garnet Red Paint, Sample #13

This sample is a steel panel spray-painted with Garnet Red Paint (Dupli-color #T-345). Subsequently, the paint was coated with a gloss-reducing finish (Plasti-kote #33, Glass Frosting Spray). The final surface is rough so no coherent reflection is observed; also, the final surface is soft, so that mechanical roughness measurements are not possible. The measured BRDFs show a uniform-diffuse component in the R channel (which comes from the subsurface color), and a forward-scattering, off-specular lobe in all three color channels. The spectral independence of the off-specular lobe implies that it is a result of first-surface scattering; this was confirmed by separate measurements of the polarized BRDF. The sample tests the ability of a model to correctly describe the observed forward scattering. We thus construct a BRDF model which includes the subsurface uniform-diffuse, first-surface directional-diffuse, and subsurface forward-scattering components:

$$f_r = f_{r,uds} + f_{r,dd} + f_{r,fs} \quad (18)$$

The model has five free parameters, k_{ud} , k_{dd} , k_{fs} , σ , and τ .

A summary of fitting results is shown in Table 2. The index of refraction was set at 1.7.

Table 2 Summary of best-fit results for Garnet Red Paint #13

Models	Param.	Fitting Results		
		R	G	B
He-Torrance	k_{ud}	0.09	0.0	0.0
	k_{dd}	0.56	0.53	0.52
	σ [μm]	0.64		
	τ [μm]	8.2		
Constructed Model	k_{ud}	0.10	0.0	0.0
	k_{dd}	0.59	0.72	0.69
	k_{fs}	1.1	1.0	1.2
	σ [μm]	0.7		
	τ [μm]	8.2		

Figure 15 displays measured and best-fit BRDF results for the R channel at five incidence angles. The regions of directionally-uniform BRDF are due to the subsurface uniform-diffuse component, which exists only in the R channel, and not in the G and B channels (see Table 2). The strong directional variations of the BRDF are due to both first-surface directional-diffuse reflection and subsurface forward scattering. These components appear in almost equal magnitude in all three color channels (see Table 2). Both BRDF models give good predictions of the first-surface directional-diffuse component. However, the secondary bump at large reflection angles (an off-specular lobe) is predicted only by the new model. This secondary bump (i.e., secondary for this sample) is due to subsurface forward-scattering. The new model correctly predicts the emergence of this secondary, off-

specular lobe. From Table 2, the multiplicative coefficient for this component is of order unity and essentially independent of color, indicating that the component arises from the clear overcoat on the Garnet Red Paint.

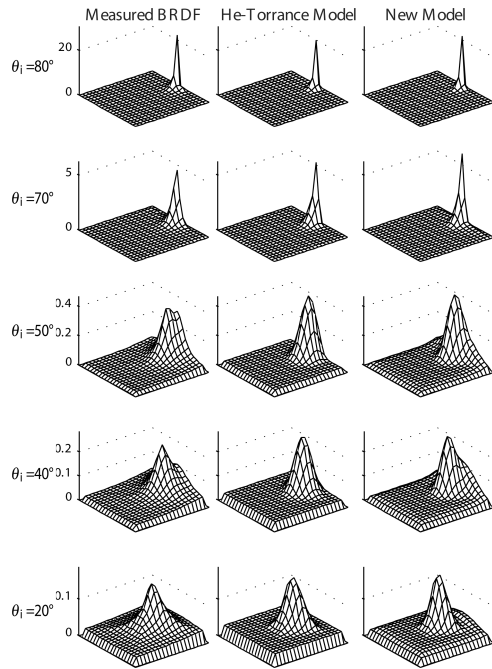


Figure 15 Comparison of best-fit curves for two BRDF models with measured BRDFs for Garnet Red Paint #13; R channel

To visually demonstrate the importance of the forward-scattering surface and subsurface lobes, consider the sphere rendered in Figure 16 with an overhead point light source. The subsurface forward scattering from the two reflection models is visibly different, and the subsurface component in the new model has a significant impact on the visual appearance.

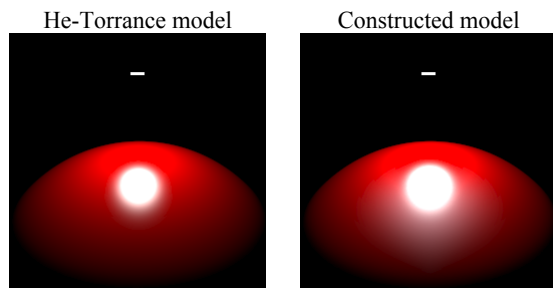


Figure 16 Images rendered with the He-Torrance and new models. The new model shows the effect of subsurface forward-scattering for Garnet Red Paint #13.

5.2.4 Laser Paper, Sample #73

This sample is a sheet of HAMMERMILL premium laser paper (24 lb. 106 brightness). We mounted the sheet on black cardboard to eliminate reflections from the mounting substrate. The incidence-plane polarized BRDFs for this sample that were discussed earlier (see Figure 6) show strong forward scattering. Hemispherical data sampling reveals that the forward scattering has large angular variations and dominates any first-surface

scattering for this surface at least until the incidence angle reaches 70°. The sample illustrates a case when the last reflection component of the new model (the subsurface forward-scattering component in equation (13)) can dominate a reflection pattern. (This term was also used in the previous section, but was not so dominant.) A summary of fitting results is shown in Table 3. The index of refraction was set to 1.5. Note that the fitting parameters are almost independent of the color channel, and that the subsurface directional-diffuse coefficient, $k_{fs}(\lambda)$, dominates the first-surface directional-diffuse coefficient, $k_{dd}(\lambda)$, in the new model.

Table 3 Summary of best-fit results for Laser Paper #73

Models	Param.	Fitting Results		
		R	G	B
He-Torrance	k_{dd}	0.73	0.75	0.64
	k_{dd}	0.45	0.39	0.38
	σ [μm]	0.54		
	τ [μm]	5.6		
Constructed Model	k_{dd}	0.91	0.94	0.83
	k_{dd}	0.28	0.25	0.25
	k_{fs}	1.9	2.0	1.7
	σ [μm]	0.39		
	τ [μm]	5.4		

In Figure 17, measured BRDFs and best-fit BRDFs for the two reflection models are shown for five incidence angles (G channel). A constant, uniform-diffuse reflection behavior dominates at large incidence angles. Both models allow for this, and also show an approximate agreement in the more dramatic directionally-varying component. The new model, for which there is both first-surface and subsurface directional forward-scattering, agrees better with the measurements. Again, the He-Torrance model fails to predict the secondary, off-specular lobes that emerge at grazing angles of view.

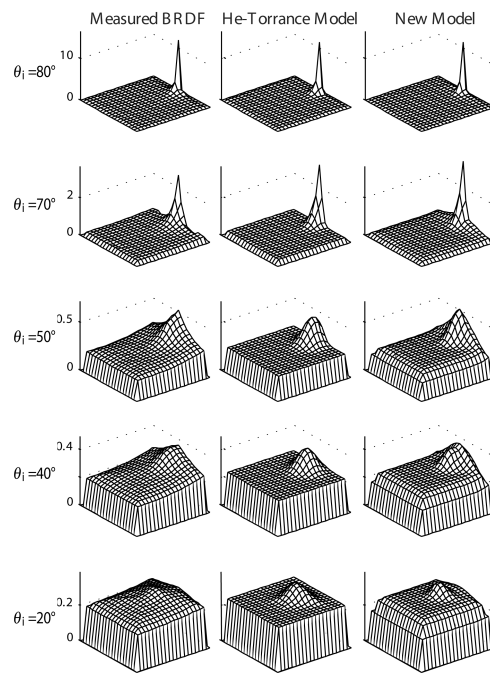


Figure 17 Comparison of best-fit curves for two BRDF models with measured BRDFs for Laser Paper #73; G channel.

5.3 Benchmarking the BRDF model

We carried out benchmarking of the new and several selected BRDF models. (Due to time, we had to limit the selection of models.) First, the selected models were best-fit to measured BRDFs for the four surfaces in Section 5.2. The result was four sets of best-fit coefficients for each model. Then, for each model and for each set of coefficients, using Java formulations, a million pairs of unit vectors in the incident and reflection hemispheres were generated with random numbers. Each pair represents one possible combination of incident and reflected directions. We calculated the BRDF values for these vector pairs. The computational time for the million BRDF evaluations is used as our measure of computational cost. Benchmarking was executed on a Pentium III 550 MHz processor, with 512MB of memory, running under the Windows XP operating system. The Java Compiler was Sun's JDK 1.4.2. The benchmarking program was run with the "-server" VM option to use a just-in-time compiler, which converts Java bytecode into machine language instructions. The running times for the BRDF depend on the input parameters for each model. For the new BRDF model, the running times also depend on which of the five components were incorporated. The results of the benchmarking are summarized in Table 4.

Table 4 Benchmarking results for various BRDF models

Model	Running Time
Blinn-Phong	1.1
Neumann-Neumann	3.5-4.0
Lafortune	2.3-3.9
Ward	2.0-2.1
Cook-Torrance	3.3-3.5
He-Torrance	59.0-121.9
Constructed models	4.3-6.8

The benchmarking shows that the new BRDF model has a computational cost comparable to the empirical and micro-facet BRDF models, and much less than the He-Torrance wave optics model.

6 Conclusion

In this work we summarize several local light scattering processes, both surface and subsurface, that have a significant impact on rendered images. Renderings illustrate some of the visual effects. A practical, comprehensive reflection model is proposed to include those processes. The model consists of five component terms. Guidelines are provided to help select the terms needed for rendering a specific surface. The physical correctness of the new model is validated against measured BRDFs. The computational cost is assessed. We conclude that the new formulation achieves an accuracy comparable to wave-optics models at a cost comparable to that of empirical and micro-facet models.

The new model incorporates all of the physical phenomena appearing in the He-Torrance model, except for polarization. Further, the new model is simpler, and also applies to anisotropic surfaces. It is of closed analytic form. Unfortunately, we cannot provide importance sampling for the new model because the cumulative distribution function of the directional-diffuse term could not be inverted. The model can be extended by adding additional BRDF components to describe phenomena that are currently beyond its scope.

Appendix: Extending the reflection model to anisotropic surfaces

For anisotropic surfaces, we assume the RMS roughness is constant and the autocorrelation length varies with the azimuthal angle. The autocorrelation function becomes:

$$C(x, y) = \exp\left(-\frac{x^2}{\tau_x^2} - \frac{y^2}{\tau_y^2}\right) \quad (20)$$

where τ_x and τ_y are autocorrelation lengths aligned with principal orthogonal axes x and y in the plane of the surface. To extend the reflection model, we need only to extend functions that depend on τ . This affects the specular reflection, first surface directional-diffuse, and subsurface forward-scattering components (Sections 3.1, 3.2 and 3.5). The RMS slopes for the directions x and y are:

$$m_{e,x} = \sigma / \tau_x, \quad m_{e,y} = \sigma / \tau_y \quad (21)$$

The modified forms of equations (10), (6), and (8) are:

$$D = \left(\frac{\vec{v} \cdot \vec{v}}{\vec{v} \cdot \vec{N}}\right)^2 \frac{\exp\left[-\frac{\tan^2 \theta_b \left(\frac{\cos^2 \phi_b}{m_{e,x}^2} + \frac{\sin^2 \phi_b}{m_{e,y}^2}\right)}{4}\right]}{16 m_{e,x} m_{e,y} (\cos \theta_i + \cos \theta_r)^2} \quad (22)$$

$$S = [1 - (1 - \cos \theta_i)^{k_i}] \cdot [1 - (1 - \cos \theta_r)^{k_r}] \quad (23)$$

$$\sigma_e = \sigma \cdot [1 - (1 - \cos \theta_i)^{1.6k_i}]^{0.1k_i} \cdot [1 - (1 - \cos \theta_r)^{1.6k_r}]^{0.1k_r} \quad (24)$$

where

$$k_i = \frac{\sqrt{\cos^2 \phi_i \tau_x^2 + \sin^2 \phi_i \tau_y^2}}{\sigma}; \quad k_r = \frac{\sqrt{\cos^2 \phi_r \tau_x^2 + \sin^2 \phi_r \tau_y^2}}{\sigma} \quad (25)$$

The forward-scattering component (equation (13)) becomes:

$$f_{r,fs} = \frac{k_{fs}}{\pi} (\lambda) T(t_\lambda, \theta_i) T(t_\lambda, \theta_r) (1 - \cos \theta_i) (1 - \cos \theta_r) \cdot \exp\left[-\frac{\tan^2 \theta_f \left(\frac{\cos^2 \phi_b}{m_{e,x}^2} + \frac{\sin^2 \phi_b}{m_{e,y}^2}\right)}{16}\right] \quad (26)$$

In Figure 18, we present predicted BRDFs for an anisotropic surface, plotted in polar coordinates for three azimuthal angles of incidence ($\phi_i = 0^\circ, 45^\circ, 90^\circ$). The RMS roughness is $\sigma = 0.5 \mu\text{m}$; the autocorrelation lengths τ_x and τ_y are $2.5 \mu\text{m}$ and $5 \mu\text{m}$. The plotted BRDFs are shown from two viewing directions.

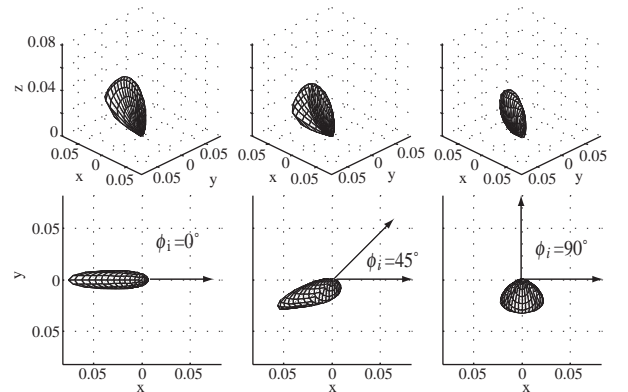


Figure 18 Polar plots of BRDFs predicted for an anisotropic surface for three azimuthal angles of incidence.

References

- ASHIKHMIN M. AND SHIRLEY P., 2000. An Anisotropic Phong BRDF Model, *Journal of Graphics Tools* 5, 2, 25-32.
- BECKMANN, P. AND SPIZZICHINO, A. 1963. The Scattering of Electromagnetic Waves from Rough Surfaces, Pergamon Press.
- BECKMANN, P. 1965. Shadowing of random rough surfaces. *IEEE Transactions on Antennas and Propagation* 13, 384–388.
- BLINN, J. F. 1977. Models of light reflection for computer synthesized pictures. In *Computer Graphics (Proceedings of ACM SIGGRAPH 77)* 11, 2, ACM, 192–198.
- CABRAL, B., MAX, N., AND SPRINGMEYER, R. 1987. Bidirectional reflectance functions from surface bump maps. In *Computer Graphics (Proceedings of ACM SIGGRAPH 87)* 21, 4, ACM, 273–282.
- COOK, R. L., AND TORRANCE, K. E. 1981. A reflectance model for computer graphics. In *Computer Graphics (Proceedings of ACM SIGGRAPH 81)* 15, 3, ACM, 307–316.
- DAVIES, H. 1954. The reflection of electromagnetic waves from a rough surface. *Proc. IEE* 101, 209–214.
- FOO, S. C., 1997. A gonioreflectometer for measuring the bidirectional reflectance of material for use in illumination computation, M.S. thesis (Cornell University, Ithaca, NY).
- GONDEK, J. S., MEYER, G. W., AND NEWMAN, J. G., 1994. Wavelength dependent reflectance functions. In *Proceedings of ACM SIGGRAPH 94*, 213–220.
- GRANBERG, H., 2003. Optical response from paper: angle-dependent light scattering measurements, modeling, and analysis, KTH Production Engineering, PhD Dissertation.
- GREENBERG, D. P., TORRANCE, K. E., SHIRLEY, P., ARVO, J., FERWERDA, J. A., PATTANAİK, S., LAFORTUNE, E. P. F., WALTER, B., FOO, S.-C., AND TRUMBORE, B., 1997. A framework for realistic image synthesis. In *Proceedings of ACM SIGGRAPH 97*, 477–494.
- HE, X. D., TORRENCE, K. E., SILLION, F. X., AND GREENBERG, D. P. 1991. A comprehensive physical model for light reflection. In *Computer Graphics (Proceedings of ACM SIGGRAPH 91)* 25, 4, ACM, 175–186.
- HE, X. D., HEYNEN P. O., PHILLIPS R. L., TORRENCE, K. E., SALESIN D. H., AND GREENBERG, D. P. 1992. A Fast and Accurate Light Reflection Model, In *Computer Graphics (Proceedings of ACM SIGGRAPH 92)* 26, 2, ACM, 253-254.
- KAJIYA, J. T. 1985. Anisotropic reflection models. In *Computer Graphics (Proceedings of ACM SIGGRAPH 85)* 19, 4, ACM, 15–21.
- KAUTZ, J., AND MCCOOL, M. D. 1999. Interactive rendering with arbitrary BRDFs using separable approximations. In *Proceedings of the 10th Eurographics Workshop on Rendering*, 281-292.
- KOENDERINK, J., AND VAN DOORN, A. 1998. Phenomenological description of bidirectional surface reflection. *J. Opt. Soc. Am. A* 15, 11, 2903–2912.
- LAFORTUNE, E. P. F., FOO, S.-C., TORRANCE, K. E., AND GREENBERG, D. P. 1997. Non-linear approximation of reflectance functions. In *Proceedings of ACM SIGGRAPH 97*, 117–126.
- LI, H. AND TORRANCE, K. E., 2003. Validation of the Gonioreflectometer, Technical Report PCG-03-2 (Program of Computer Graphics, Cornell University, Ithaca, NY)
- LI, H. 2005. Upcoming PhD dissertation.
- MATUSIK, W., PFIZER, H., BRAND, M., AND MCMILLAN, L. 2003. A data-driven reflectance model, *ACM Transactions on Graphics* 22, 3, 759–769.
- NEUMANN, L., NEUMANN, A., AND SZIRMAY-KALOS, L. 1999. Compact metallic reflectance models. *Computer Graphics Forum* 18, 13.
- NICODEMUS, F. E., RICHMOND, J. C., HSIA, J. J., GINSBERG, I. W., AND LIMPERIS, T. 1977. Geometric considerations and nomenclature for reflectance. Monograph 161, National Bureau of Standards (US), Oct.
- OREN, M., AND NAYAR, S. K., 1994. Generalization of lambert's reflectance model. In *Proceedings of ACM SIGGRAPH 94*, 239–246.
- PHONG, B.-T. 1975. Illumination for computer generated images. *Communications of the ACM* 18, 6 (June 1975), 311-317.
- POULIN, P., AND FOURNIER, A. 1990. A model for anisotropic reflection. In *Computer Graphics (Proceedings of ACM SIGGRAPH 90)* 24, 3, ACM, 267-282.
- SCHLICK, C. 1994. An inexpensive BRDF model for physically-based rendering. *Computer Graphics Forum* 13, 3, 233-246.
- SCHRÖDER, P., AND SWELDENS, W., 1995. Spherical Wavelets: Efficiently Representing Functions on the Sphere,” In *Proceedings of ACM SIGGRAPH 95*, 161-172.
- SHIRLEY, P., AND CHIU, K., 1994. Notes on adaptive quadrature on the hemisphere, Technical Report 441, Department of Computer Science, Indiana University, Bloomington, IN.
- SHIRLEY, P., HU, H., SMITS, B., AND LAFORTUNE, E. 1997. A practitioners' assessment of light reflection models. In *Pacific Graphics* 97, 40–49.
- SILLION, F. X., ARVO, J. R., WESTIN, S. H., AND GREENBERG D. P., 1991. A global illumination solution for general reflectance distributions, In *Computer Graphics (Proceedings of ACM SIGGRAPH 91)* 25, 4, ACM, 187–196.
- SMITH, B. G., 1967. Geometrical shadowing of a random rough surface. *IEEE Transactions on Antennas and Propagation* 15, 668–671.
- STAM, J. 1999. Diffraction shaders. In *Proceedings of ACM SIGGRAPH 99*, 101–110.
- STOGRYN, A., 1967. Electromagnetic Scattering From Rough, Finitely Conducting Surfaces, *Radio Science* 2, 4, 415-428.
- TORRANCE, K. E., AND SPARROW, E. M. 1967. Theory for off-specular reflection from roughened surfaces. *Journal of Optical Society of America* 57, 9, 1105-1114.
- WARD, G. J. 1991. Measuring and modeling anisotropic reflection. In *Computer Graphics (Proceedings of ACM SIGGRAPH 91)* 25, 4, ACM, 265–272.
- WESTIN, S. H., ARVO, J. R., AND TORRANCE, K. E. 1992. Predicting reflectance functions from complex surfaces. In *Computer Graphics (Proceedings of ACM SIGGRAPH 92)* 26, 2, ACM, 255–264.
- WOLFF, L. B., NAYAR, S. K., AND OREN, M., 1998. Improved Diffuse Reflection Models for Computer Vision, *IJCV* 30, 1, 55-71.